Icarus 455 (2026) 117105

Contents lists available at ScienceDirect

Icarus

journal homepage: www.elsevier.com/locate/icarus

Tracking the untrackable: Reconstructing a Soyuz-2.1b re-entry trajectory using inter-disciplinary observations☆

Isabella R. Hatty [a,b,*], Eleanor K. Sansom [a,b], Hadrien A.R. Devillepoix [a,b], Trent Jansen-Sturgeon [c], Martin C. Towner [a,b], Iona Clemente [a,b]

[a] Space Science and Technology Centre, Curtin University, GPO Box U1987, Perth, 6845, WA, Australia
[b] International Centre for Radio Astronomy Research, 1 Turner Avenue, Perth, 6102, WA, Australia
[c] Lockheed Martin Australia, 5 Third Ave, Mawson Lakes, Adelaide, 5095, SA, Australia

ARTICLE INFO

Keywords:
Atmospheres, dynamics
Orbit determination
Satellites, atmospheres
Satellites, composition
Satellites, dynamics

ABSTRACT

When launch vehicles rise through the atmosphere and jettison their stages to place spacecraft in orbit, the first few stages often fall back down to Earth into areas bounded by Notice to Air Missions (NOTAMs). These are known as scheduled space debris re-entries. The amount of scheduled debris, and therefore NOTAMs, depends on the launch vehicle and target orbit. The true impact areas of scheduled debris are often unconfirmed due to a global lack of observational coverage below 200 km. A suite of observational capabilities exist within Australia, though none are specifically designed or designated for re-entries, they incidentally observe these events as they are carrying out their primary functions. At 13:20:00z on 7 August 2023, a Soyuz-2.1b was launched from Plesetsk Cosmodrome, carrying a first-of-its-kind COSMOS 2569 navigation satellite. 36 min after launch, the Desert Fireball Network observed a fireball over Victoria, Australia. Seismic stations from the Australian National Seismograph Network and infrasound arrays from the Australian infrasound network observed ballistic trajectory signals over Victoria and Tasmania. This collection of interdisciplinary observations provided a unique opportunity to reconstruct the trajectory and assess energy deposition of a scheduled re-entry using our methods designed for meteors, such as the Dynamic Trajectory Fit method. We estimated an overall average surviving mass of 1980 kg, with gradual fragmentation over the Bass Strait that separated the object into at least three main fragments. We verified that the object splashed down within the NOTAM danger area, 24 km off the Tasmanian coast.

1. Introduction

1.1. Natural vs. artificial origins of fireballs

Fireballs are unusually bright meteors. Those of natural origin result from large meteoroids entering Earth's atmosphere at high speeds, while those of artificial origin are from re-entering space debris. The behavior of natural meteoroid entries is an extensively researched field (Sansom et al., 2018, 2017; Devillepoix et al., 2022), while artificial debris research is limited in the public domain. We recognize that debris re-entry analysis is a multi-physics problem, but the same datasets and techniques being used to research natural fireballs have proven to be highly effective in capturing debris (Šilha et al., 2023; Zigo et al., 2025). Gravitational force and atmospheric drag are more pronounced for debris with less kinetic energy and shallower entry angles, but they both exhibit the same two phases of bright and dark flight. Bright flight is the luminous, fireball phase and occurs in the hypersonic regime where extreme atmospheric deceleration causes ablation of the object and visible atmospheric ionization. Visible ionization requires extreme excitation, whereas ablation depends only on sufficient heat; consequently, mass-loss can persist even after bright flight has ended. The extent to which ablation continues beyond bright flight is strongly material dependent, governed by thermophysical properties, such as melting temperature, heat of ablation, and thermal conductivity, which control whether the residual heat flux remains sufficient to sustain ongoing mass-loss.

Dark flight follows when the fireball phenomenon ceases and any remaining objects fall to the ground, severely affected by atmospheric winds. As the object decelerates, its velocity becomes comparable to that of the surrounding airflow, and its motion transitions from momentum-dominated to increasingly governed by atmospheric winds. We wish to explore insights into re-entry mechanics and fragment

☆ This article is part of a Special issue entitled: 'Meteoroids 2025' published in Icarus.

* Corresponding author at: Space Science and Technology Centre, Curtin University, GPO Box U1987, Perth, 6845, WA, Australia.
E-mail address: isabella.hatty@postgrad.curtin.edu.au (I.R. Hatty).

https://doi.org/10.1016/j.icarus.2026.117105
Received 31 January 2026; Received in revised form 28 March 2026; Accepted 14 April 2026
Available online 17 April 2026

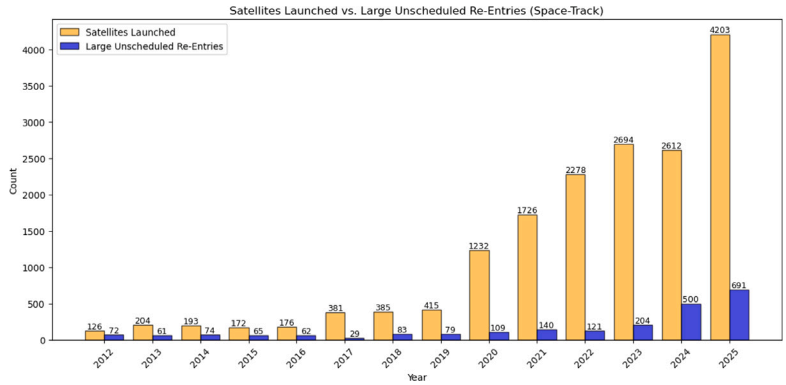

Fig. 1. The increasing frequency of launches and corresponding unscheduled, large re-entries since 2012. Data as of 3 January 2026.

survivability that may affect impact areas and reliability of re-entry risk assessments using our methods designed for meteors. We believe that meteor and debris re-entry studies are synergistic, with developments in each informing the other. Parigini et al. (2013) demonstrated this synergy by applying classical debris re-entry analysis methods to asteroid entry and validating their applicability.

1.2. State of space

With tens of thousands of satellites expected to be launched by 2050, space debris in low Earth orbit (LEO) is an ever increasing problem (Wright et al., 2024). Most pieces of debris are too small to survive re-entry, and burn up in Earth's atmosphere. However, larger pieces are known to survive re-entry and impact the ground.

There are two types of re-entries: unscheduled and scheduled. Unscheduled re-entries are uncontrolled and of orbital origin, including defunct satellites, pieces of debris from collisions and discarded rocket bodies. Larger pieces of unscheduled debris have survived re-entry and impacted towns, farms, and homes around the world for over 40 years (The Aerospace Corporation, 2026). To date, there have been no casualties, but with the increasing frequency of these events, so is the risk. The United States Space Command manages a website, known as Space-Track.org, that provides predictions for unscheduled re-entries (Space-Track.Org, 2026). Fig. 1 shows the relationship between the increased frequency of launches and unscheduled, large re-entries using Space-Track data. Both cases show a record count in 2025 with 588 of the 691 re-entries corresponding to Starlink satellites.[1]

Scheduled re-entries rely on Notice to Air Missions (NOTAMs) for disseminating risk assessment. They can be rocket stages, i.e. fuel tanks, that are jettisoned from the main rocket once fuel is spent during its ascent into orbit. They are known to survive re-entry and have associated danger areas or NOTAMs that are usually over oceans to minimize risk to people and property. NOTAMs are issued by aviation authorities and provide time-sensitive airspace restrictions for aircraft and sea vessels. In the case of scheduled re-entries, NOTAMs provide a temporary "no-fly/sail" area for risk of falling debris. According to the Australian Space Agency (ASA) and as of 12 November 2025, Australia received 108 NOTAMs within its flight information region (FIR) in 2025 due to jettisoned rocket stages, more than double the count in 2023 (Fig. 2). The main actors are launching satellites into highly inclined, sun synchronous orbits from Central Asia. Launch failure and debris falling outside dedicated danger areas is also possible, seen recently when debris from a Long March 2C rocket fell near a village in South-West China on 22 June 2024 (Gan et al., 2024). Space surveillance performance degrades significantly at very low altitudes, where reduced surveillance volume limits observational coverage; even at ~250 km, tracking is described as challenging (Lee et al., 2025). As a result, re-entries are usually unobserved below 200 km. If they are unobserved, then there is no way to verify that they are falling within designated NOTAM danger areas without rocket telemetry. Russian rocket telemetry is not publicly available. Additionally, there is no global standard for NOTAM generation.

1.3. Soyuz-2.1b

The Soyuz-2.1b is a Russian, medium-lift, expendable launch vehicle that is an evolution of the long-standing Soyuz rocket family (Zak, 2025). On 7 August 2023, a Soyuz 2.1b rocket was launched from Plesetsk Cosmodrome carrying the COSMOS 2569 satellite. The second stage has a height of 27.1 m and diameter of 2.95 m. Its cylindrical shape contains two fuel tanks made of aluminum alloy, providing a total empty mass of 6545 kg.

Airservices Australia issued a NOTAM for the second stage re-entry covering an area of 161,000 km^2 and opening between 13:00:00z–16:00:00z on 7–9 August, 24 km off the Tasmanian coast. Sensors from the Desert Fireball Network (DFN) in Australia, Australian National Seismograph Network (ANSN) and infrasound network recorded the suborbital flight of this scheduled re-entry, showing how these datasets can fill the gap in observational coverage below 200 km (Lee et al., 2025).

2. Datasets

A range of unconventional instruments exist within Australia that are able to passively record re-entering space debris, including the DFN, ANSN and sensors from the Australian infrasound network or International Monitoring System (IMS). Although these datasets differ significantly, their combined use enables comprehensive characterization of re-entry trajectories. In an ideal scenario, a single re-entry event would be observed across all systems to maximize coverage. In this case, we acquired observations of the Soyuz-2.1b re-entry from the DFN, ANSN and the Australian infrasound network.

2.1. Desert fireball network

The DFN is a distributed array of sensors across the remote Australian outback. The digital DFN from 2015–2024 consisted of over 50 automated observatories, covering an area of 5×10^7 km^2 across West and South Australia, Victoria and New South Wales. The primary objectives of the DFN are to recover meteorites and determine their orbital origins in our solar system. Astrometric data collected by specialist camera systems and purpose-built, high-precision atmospheric

[1] Space-Track classifies "large" as objects with cross-sectional areas larger than 1 m^2.

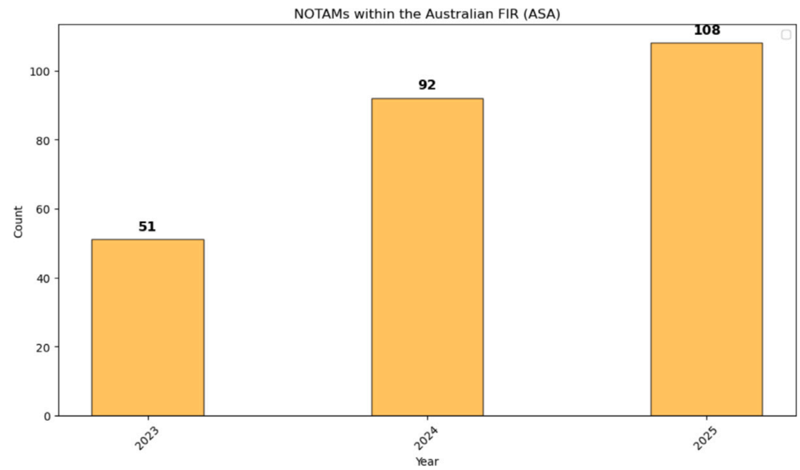

Fig. 2. Australia received 108 NOTAMs within its FIR due to jettisoned rocket stages in 2025, more than double the count in 2023. Data as of 12 November 2025.

modeling software is used within trajectory models to predict constrained fall zones. Within predicted fall zones, unmanned aerial vehicle (UAV) surveying is used, coupled with machine learning techniques, to automatically identify meteorite candidates.

Due to its operating time-area, the DFN has produced a large dataset of triangulated fireballs, with approximately 1500 events having derived trajectories and orbits using the methods described in Section 3 (Towner et al., 2021). Two newly installed DFN cameras in Victoria captured nearly 70 s of the Soyuz-2.1b re-entry. A roughly north–south trajectory was observed over land, before it went beyond the field-of-view of these two camera stations.

2.1.1. Astrometric data

The DFN camera system is comprised of a 36 MPixel Nikon D810 sensor combined with an 8 mm F/3.5 SAMYANG fisheye lens giving an all-sky view. Fireballs are captured by the DFN through 27 s long exposure images taken every 30 s throughout the night. Fig. 3 shows multiple stacked long exposure images of the Soyuz-2.1b re-entry as captured by DFN cameras at Invergordon and Stanhope. A liquid crystal (LC) shutter installed between the lens and the sensor modulates light, encoding absolute timing at an average of 15 Hz into every image by use of a de Bruijn sequence. Microcontrollers synced with Global Navigation Satellite Systems (GNSS) enable temporal synchronization across the entire DFN to an absolute timing accuracy of 0.4 ms (Howie et al., 2017). The background star field provides astrometric calibration to allow conversion from pixel to sky coordinates, i.e., x, y in an image to altitude and azimuth (Devillepoix et al., 2018).

2.1.2. Atmospheric data

Dark flight refers to the free-fall period once the visible phenomenon ceases. During this phase, atmospheric winds and density variations strongly influence the descent of surviving debris, often shifting fall zones by several kilometers, and therefore require high-precision modeling. The DFN performs dark flight calculations using the Advanced Research Weather Research and Forecasting (WRF) model, developed by the National Center for Atmospheric Research (NCAR) (Skamarock et al., 2008). The WRF model can assimilate observational data, such as radiosonde balloon measurements, to produce high-resolution simulations up to 30 km. Rather than forecasting, the DFN uses historical measurements to "hindcast" atmospheric conditions at the time of re-entry, with a focus on the predicted fall zone.

2.2. Australian national seismograph network

Geoscience Australia (GA) operates ANSN, comprising of over 100 seismic stations across Australia. Although primarily designed for earthquake monitoring, the ANSN can also detect re-entering space debris. If debris survives to the lower atmosphere and remains sufficiently large, it generates shock-waves (Bronshten, 1964; ReVelle, 1976, 2008; Silber and Brown, 2019) that propagate through the atmosphere. These shock-waves, perceived as sonic booms, can couple into the ground and be recorded as seismic signals (Fernando et al., 2024). When combined with other datasets, such observations help constrain the timing and energy of the re-entry. The ANSN provides continuous (24 hr) coverage and can detect signals while the body remains supersonic, even during dark flight. The typical sensing range for re-entering debris is on the order of 250 km (Neidhart et al., 2021). However, spatial resolution is limited as heavy anthropogenic noise, such as human activity, roads and industrial buildings, can hide the shock-wave signal (Fernando et al., 2024).

2.3. Australian infrasound network

The Comprehensive Nuclear-Test-Ban Treaty Organization's IMS includes an Australian network of infrasound arrays. Each array includes several microbarometers – effectively sensitive microphones – designed to measure low-frequency (0.01–20 Hz) atmospheric pressure variations produced by explosions. IMS arrays can record the sonic boom or shock-wave from re-entering space debris at ranges from a few hundred kilometers up to global distances (depending on energy and atmospheric conditions) (Fernando et al., 2024). Arrays are configured to ensure that signals arriving at different angles produce measurable time delays between the array's elements, allowing polarization of the signal (its direction of arrival) to be determined (see Section 4.2). They also have 24 hr coverage and record signals while the body remains supersonic. However, propagation is strongly temperature and wind-dependent. Atmospheric conditions, such as temperature gradients and wind layers, can cause refraction away from arrays, resulting in shadow zones where the signal is not recorded. When used with other datasets, infrasound signals can provide independent timing and inferred masses for further processing.

3. Bright flight

The methods described here use bright flight observations of space debris re-entry in Bayesian modeling. The object is hypersonic during this phase and quickly decelerating, causing intense aerodynamic heating and often fragmentation.

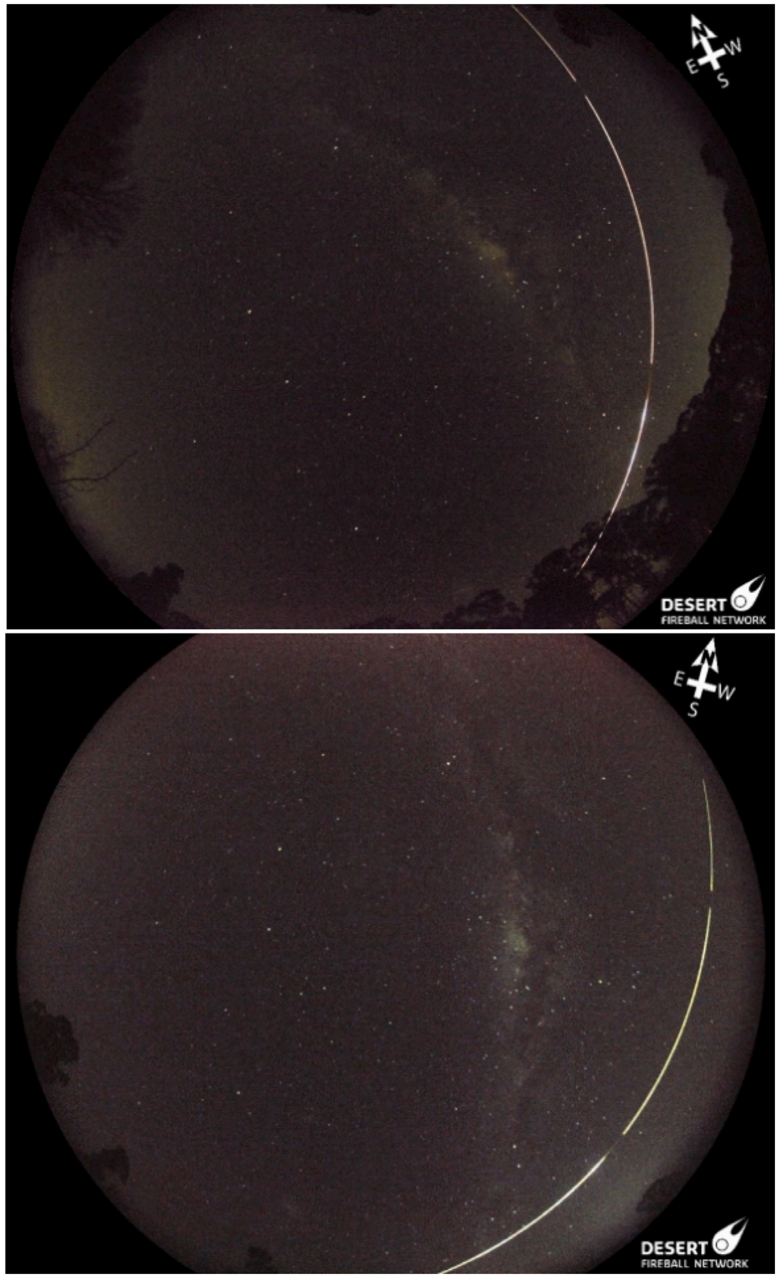

Fig. 3. Images of the Soyuz-2.1b re-entry as captured by DFN cameras at Invergordon (above) and Stanhope (below). These images are stacks of three 27 s, long-exposure images. The gaps are caused by the 3 s exposure of the shutters between frames.

The most common methods for reconstructing natural fireball trajectories assume a straight-line trajectory (Sansom et al., 2018). This is acceptable for the relatively short (<10 s), steep (∼45°), and fast (11–72 km/s) meteors. This is not the case for re-entries that are usually longer (>30 s), shallower (1–2°) and slower (<11 km/s), and for which there are greater gravitational and atmospheric effects to consider. The Dynamic Trajectory Fit (DTF) method by Jansen-Sturgeon et al. (2020) removes this assumption by fitting the following differential equations of motion and ablation directly to the measured lines-of-sight using our astrometric data:

$$\frac{d\vec{v}}{dt} = -\frac{\rho_a \|\vec{v}_{\rm rel}\|}{2B}\vec{v}_{\rm rel} + \vec{a}_g \quad (1)$$

$$\frac{dB}{dt} = -\frac{\sigma \rho_a \|\vec{v}_{\rm rel}\|^3}{6} \quad (2)$$

Where $\vec{v}$ is the object's absolute velocity in the Earth-Centered Inertial (ECI) frame, $\vec{v}_{\rm rel}$ is the velocity relative to the atmosphere, a_g is the acceleration due to gravity and ρ_a is atmospheric air density calculated using the NRLMSISE-00 empirical atmospheric model (Picone et al., 2002). B is a ballistic coefficient, defined as $B = \frac{m}{c_d S_c}$, where m is the mass, c_d is the drag coefficient and S_c is the cross-sectional area. σ is the ablation coefficient, defined as $\sigma = \frac{c_h}{c_d H^*}$, where c_h is the heat-transfer coefficient and H^* is the enthalpy of sublimation.

Jansen-Sturgeon et al. (2020) provides a conceptual overview of the DTF method with sufficient detail for reproducibility. The overview presented here addresses all modifications that we have applied to this method in order to better model re-entering debris, using the Soyuz-2.1b re-entry as a case study. The DTF method is divided into three main parts: state approximation, sanity checks and optimization.

Table 1
Estimated initial physical parameters.

Parameter	Value	Source
Object Mass	6545 kg	Kiseleva (2022)
Object Radius	1.475 m	Kiseleva (2022)
Object Height	27.1 m	Kiseleva (2022)
Object Density (ρ)	2813 kg/m^3	Aluminium AA7075 (Vovk et al., 2023)
Cross-Sectional Area (S_c)	79.95 m^2	Calculated
Drag Coefficient (c_d)	1	Although the diameter-to-length (D/L) ratio is <0.2, c_d is approximated as 1 in a continuum flow (<80 km) (Kanzler et al., 2019)
Initial Ballistic Coefficient (B^i)	81.87	Calculated
Heat Transfer Coefficient (c_h)	0.284 W/m^{2}K^1	Vovk et al. (2023)
Enthalpy of Sublimation (H^*)	1.22 × 10^7 J/kg^1	Bronshten (1964)
Ablation Coefficient (σ)	2.32 × 10−8 s^2/m^2	Calculated

3.1. State approximation

The traditional DTF method focuses on fitting the state at the end of the bright flight trajectory, where parameters (such as mass, size, shape, and material composition) are better constrained for meteoroids. However, for space debris, these parameters are better constrained at the beginning of the trajectory. The estimated parameters describe the dynamics of the object at the beginning of the trajectory, as in Eqs. (1) and (2). The collection of these parameters defines the object's "state" and is given by the following vector:

$$\vec{\chi}_{\text{est}} = \left[p^i_x, p^i_y, p^i_z, v^i_x, v^i_y, v^i_z, B^i, \sigma, \Delta t_j, t^{rel}_k\right]$$

The first eight parameters define the trajectory, where $[p^i_x, p^i_y, p^i_z]$ is the initial position, $[v^i_x, v^i_y, v^i_z]$ is the initial velocity, B^i is the initial ballistic coefficient and σ is the ablation coefficient. If one or more cameras have timing offsets, an estimated offset time, Δt, is added to the state for every offset camera. Finally, if one or more fireball lines-of-sight are recorded without relative timing, an estimated relative time, t^{rel}, is approximated during modeling, for every line-of-sight that lacks timing information.

From here, we build up from the Method of Planes (MOP) (Ceplecha, 1987) to the Straight Line Least-Squares (SLLS) (Borovička, 1990) method using these rough timing corrections to estimate initial position and velocity parameters. The estimated position is merely the initial triangulated point along the SLLS line, and the estimated velocity is a least-squares average velocity of the first eight triangulated positions. For the Soyuz-2.1b, some initial parameters were set assuming an aluminum alloy cylinder falling side-down in a continuum flow. The initial ballistic coefficient, B^i, and ablation parameter, σ, were estimated using the physical parameters in Table 1 to give B^i ∼81.87 kg/m^2 and σ ∼2.32e^{-8} s^2/m^2. The purpose of the initial state is to start the optimization sufficiently close to the global minimum to allow successful convergence.

3.2. Sanity checks

The second step involves a variety of sanity checks to remove erroneous data before optimization is attempted. All sanity checks applied to the SLLS fit and initial state approximation of natural fireball observations described by Jansen-Sturgeon et al. (2020) also apply to re-entering space debris, e.g., triangulate to positions above the ground. However, we allow observations of re-entering debris to increase in height over time and the rate of this change to vary. This is to account for external forces that may be more significant than in natural fireballs. If a sanity check fails, the camera is removed and the flow restarts from state approximation.

Table 2
State boundary given to the least-squares algorithm to ensure realistic results. *Represents the associated estimated state parameter as determined in state approximation.

State parameter	Lower bound	Upper bound
$\vec{p}^f$ (km)	−40*	40*
$\vec{v}^f$ (km/s)	−5*	5*
B (kg/m^2)	10^{-10}	10^4
σ (kg/J)	3e^{-9}	1
t^{rel} (s)	−10*	10*
Δt (s)	−10*	10*

3.3. Optimization

The final step performs a minimization routine using SciPy's least-squares function. The function uses the Trust Region Reflective (TRF) method to impose lower and upper bounds on the optimized state (Table 2). The bounds are generous to give the minimization routine enough room to search the state-space while keeping the resulting state realistic. The TRF method also has a parallelized Jacobian function that uses central differencing to estimate derivatives.

The optimized state is now propagated using Eqs. (1) and (2) to all other observation times and subsequently converted to lines-of-sight. The Jacobian calculates angular in-track and cross-track residuals between fitted and observed lines-of-sight, highlighting the direction towards local minimum. The state parameters are iteratively adjusted to minimize these angular residuals until the state does not differ significantly from one iteration to the next; indicating that we have reached a minimum and the resulting state matches the observations as closely as possible. The DTF method also outputs KMZ files for visualization of reconstructed trajectories in geospatial software, such as Google Earth.

In addition to estimating dynamic parameters, we also simultaneously estimate some physical parameters. By assuming a constant shape factor, A_s, and density, ρ, the fitted B can be used to estimate the mass of the object, m_{est}, throughout its luminous trajectory. m_{est}, is calculated using Eq. (3) and the parameters in Table 1. The uncertainty in m_{est} is calculated using first-order error propagation.

$$m_{est} = \frac{(Bc_d A_s)^3}{\rho^2} \tag{3}$$

Finally, errors on the dynamic and physical parameters of the state are estimated and saved for subsequent dark flight modeling. The least-squares algorithm used within the DTF method does not produce formal uncertainties. Jansen-Sturgeon et al. (2020) details how overall covariance errors are estimated from both the Jacobians of the optimized state and the line-of-sight residuals. The uncertainty formulation does not account for errors from Eqs. (1) and (2), nor the assumptions made within this model, such as a constant shape, density and ablation coefficient. Therefore, the estimated overall covariance can be thought of as a minimum bound.

4. Dark flight

Dark flight in this case refers to the period of space debris free-fall once the fireball phenomena cease. The shape and orientation of surviving space debris, as well as atmospheric winds and density variations, strongly influence fall zones. Devillepoix et al. (2018) and Sansom et al. (2020) describe the DFN's dark flight calculation methods in detail. The overview presented here addresses all modifications that we have applied to this method for re-entering debris, using the Soyuz-2.1b re-entry as a case study.

The final state of bright flight initializes the dark flight calculation. A number of virtual particles with varied mass, density, and shape factor are generated within the modeled uncertainty surrounding the final state. In the case of the Soyuz-2.1b re-entry, bright flight likely continued over the Bass Strait and beyond the DFN's field-of-view. A fifth-order explicit Runge–Kutta integrator is used to predict the continuation of flight using differential equations of motion (Eq. (1)) and mass-loss (Eq. (4)). This allows us to model continued bright flight and the transition into dark flight. We run this model using the NRLMSISE-00 empirical atmospheric model down to an altitude of 30 km. Below 30 km, as precise atmospheric conditions become more relevant, the integrator transitions to modeled atmospheric profiles from WRF, with the final results being probability heat maps that are representative of possible impact areas on the ground.

$$\frac{dm}{dt} = -\frac{\sigma c_d A_s \rho_a \|\vec{v}_{\rm rel}\|^3 m^{2/3}}{2\rho^{2/3}} \quad (4)$$

4.1. Seismic processing

ObsPy is an open-source Python library for processing and analyzing seismic data, including ANSN data. We identify which ANSN stations are within range of a given space debris re-entry using the DFN trajectory. Clemente et al. (2025) provides a detailed reduction and analysis of seismic signals from the Soyuz 2.1b re-entry.

4.2. Array processing

Similarly to seismic processing, we identify which IMS infrasound arrays are within range of a given space debris re-entry using the DFN trajectory. Once ballistic trajectory signals are identified, array processing extracts the signal arrival time, back-azimuth (apparent direction) and slowness (apparent speed across the array). From this we can approximate the range to the source. We approximate origin sources along the DFN trajectory using these measurements. We also ensure that the signal can cover the distance traveled in the delta between arrival time and source origin as an additional sanity check. Additionally, the period (T) of the signal can be used to estimate the acoustic energy ($E_{acoustic}$) using the energy deposition Eq. (5) of Silber et al. (2025), derived from meteors.

We use the velocity at the source location along the DFN trajectory, and $E_{acoustic}$ to estimate an inferred mass (m_{inf}) of the object from the kinetic energy Eq. (6). The inferred mass is the equivalent mass an object would need to produce the observed signal. Only a small, unknown fraction of kinetic energy is converted to infrasound and reaches the array during re-entry; therefore, m_{inf} represents a small, unknown fraction of the true mass and reflects how efficiently an object couples energy into the atmosphere. This provides independent timing and energy deposition for further dark flight processing.

$$\log(E_{acoustic}) = 3.30\log(T) - 1.89 \quad (5)$$

$$m_{inf} = \frac{2E_{acoustic}}{v^2} \quad (6)$$

5. Results and discussion

Sensors from the DFN, ANSN and Australian infrasound network observed the Soyuz-2.1b re-entry. Here we present our reconstructed trajectory and discuss the implications for fragmentation timing and energy deposition in parallel to the findings of Clemente et al. (2025).

5.1. Bright flight results

Two DFN cameras in Victoria (Invergordon and Stanhope) captured the Soyuz-2.1b re-entry across three long-exposure images between 13:56:14z–13:57:22z. The total observation time was 68.5 s Our global trajectory solution was generated using the modified DTF approach with all astrometric data. A reasonable global fit for dynamic parameters was achieved, and gave an approximately 450 km long trajectory over Southern Victoria.

The fireball was first observed at a height of 80.63 km and velocity of 7.84 km/s, all of our results are measured in the Earth-Centered Inertial (ECI) frame. It passed over Melbourne at a height and velocity of 65 km and 6.77 km/s before continuing over the Bass Strait towards Tasmania and beyond the DFN's field-of-view. The final observed height and velocity was 66.04 km and 6.45 km/s (Fig. 4). Velocity errors for this global fit are on the scale of ±0.04 km/s on entry to ±0.25 km/s on exit (Fig. 5).

Cross-track residuals are a good indicator of trajectory fit. The DFN typically observes cross-track residuals of natural fireballs on the scale of hundreds of meters. However, the cross-track residuals in this case show total offsets of over 8 km (Fig. 6). This is not attributable to observational uncertainties, but is more likely due to unmodeled aerodynamic effects, such as Magnus-induced lift (see Section 5.3.1.)

In an effort to improve our trajectory fit and reduce cross-track residuals, we regenerated our trajectory solution in segments. We segmented according to natural breaks in image exposures. Segment 1 being 12.8 s at the beginning, segment 2 being 26.7 s in the middle and segment 3 being 22.4 s at the end of the observed trajectory. The segmented trajectory solution estimated the entry height and velocity as 73 km and 7.3 km/s and exit as 64.13 km and 6.29 km/s, lower and slower than the global trajectory solution (Table 3). This approach improved velocity errors (Fig. 7) and reduced cross-track residuals to less than 1 km (Fig. 8). Although there are some incompatibilities in height estimates where segments join, we consider this our main trajectory solution.

Finally, in order to better understand the sensitivities of constant physical parameters (density (ρ), cross-sectional area (S_c), heat transfer coefficient (c_h) and enthalpy of sublimation (H^*)) on the final bright flight state, we re-examine segment 3. Lower and upper bounds were set by regenerating trajectory solutions using the minimum and maximum values from Table 1.

S_c was found to be the most sensitive parameter, while minimum and maximum values for ρ (2313–3313 kg/m^3), c_h (0.284–0.35 W/m^{2}K) and H^* (4.5e^5–1.22e^7 J/kg) had negligible impact on the final velocity (6.29 ± 0.1 km/s), cross-track residuals ([−600, 300] m), and final mass estimates (within ±13 kg). The minimum value for S_c (6.83 m^2, falling face-down) resulted in a completely ablated object over Victoria which is inconsistent with ballistic trajectory signals observed over Tasmania. We decided to use the maximum value for S_c (79.95 m^2, falling side-down) as it provided a reasonable final mass estimate, minimal cross-track residuals and endpoint parameters of our final observation to initialize dark flight, shown in Table 4.

5.2. Dark flight results

We used the endpoint parameters in Table 4 to initialize dark flight and predict the final trajectory path over the Bass Strait. It should be noted that bright flight likely continued beyond this endpoint (last observed point before going beyond the DFN's field-of-view) and

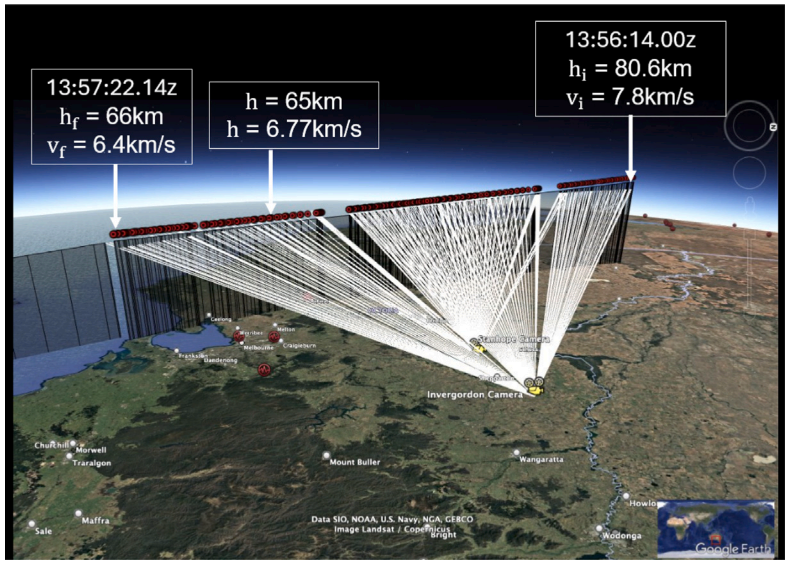

Fig. 4. Global trajectory solution for 68.5 s of the Soyuz-2.1b re-entry trajectory between 13:56:14z–13:57:22z.

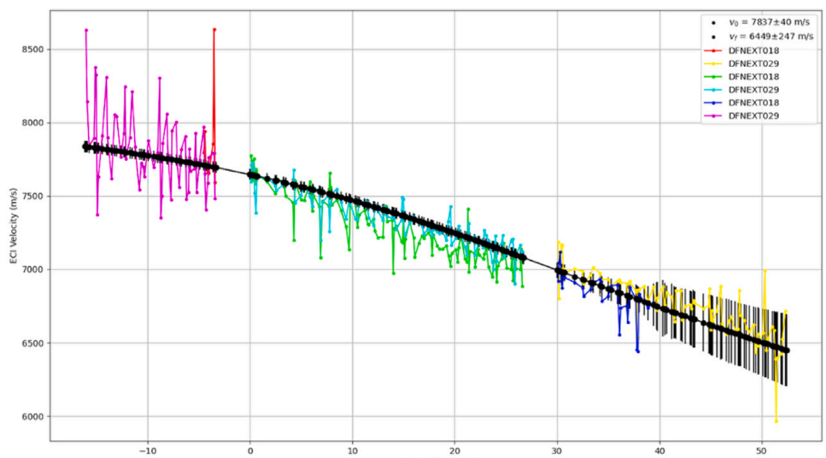

Fig. 5. ECI velocity vs. time from our first observation, showing a reasonable global fit for dynamic parameters with velocity errors on the scale of ±0.04 on entry to ±0.25 km/s on exit. The label includes observing camera name.

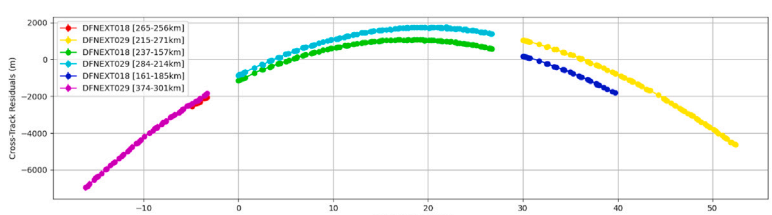

Fig. 6. Cross-track residuals for our global trajectory solution showing significant offsets over 8 km. The label includes observing camera name and proximity to the fireball.

Table 3
Comparison of segments within the main and global trajectory solutions.

Segment	1	2	3	Global
Duration (s)	12.8	26.7	22.4	68.5
Initial Height (km)	73.00	73.29	70.00	80.60
Initial Velocity (km/s)	7.30	7.60	7.29	7.80
Final Height (km)	72.63	69.83	64.13	66.00
Final Velocity (km/s)	7.70	7.38	6.29	6.40
Cross-Track Residuals (m)	[−100,100]	[−1,000,600]	[−600,300]	[−6,000,2,000]
Final Mass Estimate (kg)	≫ 6,545	≫ 6,545	2,041 ± 665	≫ 6,545

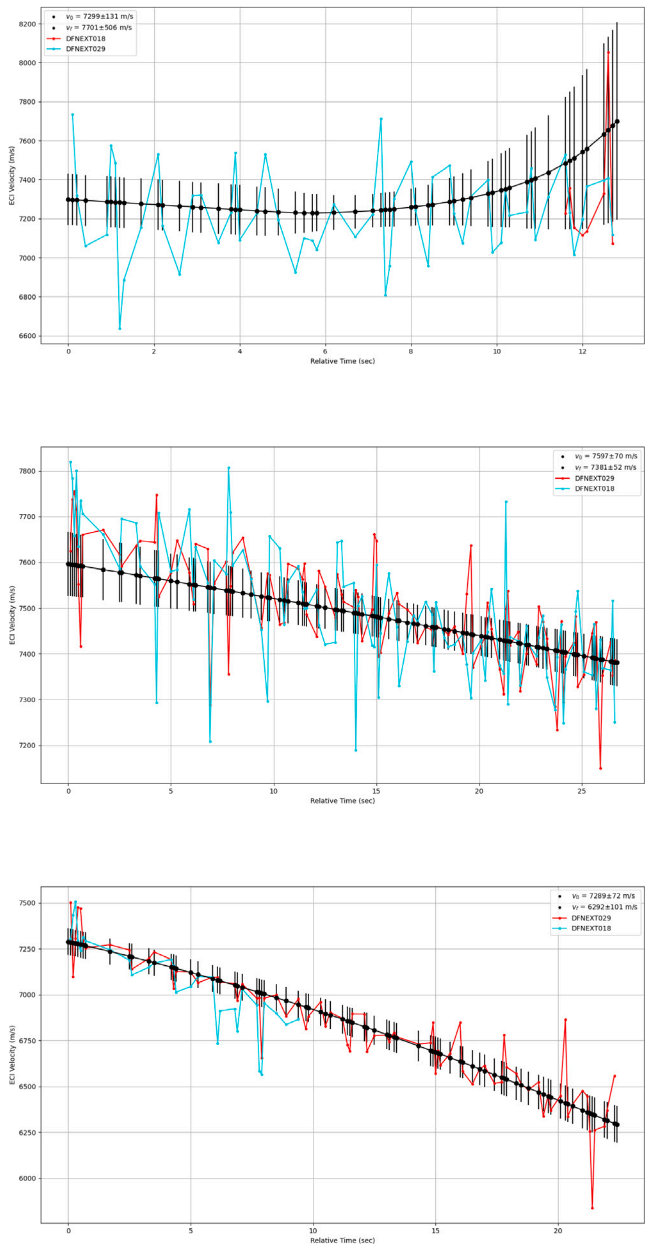

Fig. 7. ECI velocity vs. time from the beginning of segments 1 (top), 2 (middle), and 3 (bottom) showing stronger fits for dynamic parameters. The label includes observing camera name.

Table 4
Endpoint parameters of our final observation for dark flight initialization.

Endpoint parameter	
Mass (kg)	2,041
Density (kg/m^3)	2,813
Latitude, Longitude	−38.55, 144.84
Height (km)	64.13
Velocity (km/s)	6.29
Flight Path Angle (°)	−1.43
Azimuth (°)	142.65

this extended portion is accounted for in our dark flight model (see Section 4). We ran one thousand Monte Carlo simulations, varying the starting mass and density by 500 kg and 500 kg/m^3 around the fitted values. The shape factor was also varied between 0.6–1.6 to reflect the transition from a hypothetical circular cylinder to a flat plate. In all cases, the main body passed over the north-east of Tasmania at a height and velocity of approximately 48.5 km and 5.72 km/s. The average surviving mass was 1980 kg with lower and upper estimates of 1672 kg and 2853 kg. All simulations splashed down within the designated NOTAM danger area around 14:01:03z, as shown in Fig. 9. The total duration of dark flight was 3 min and 40 s, making the duration of our entire trajectory 4 min and 48.5 s.

Table 5
Timing and inferred masses of the three ballistic trajectory signals from the I05AU infrasound array in Tasmania using array processing.

Signal	1	2	3
Arrival Time	14:02:24z	14:03:14z	14:03:34z
Back-Azimuth (°)	51.7	30.6	21
Energy (J)	3.93 4 $\times 10^8$	1.21 $\times 10^8$	9.28 $\times 10^8$
Source Origin	13:58:53z	13:58:41z	13:58:35z
Distance Traveled (km)	91.8	96.8	106.4
Velocity (km/s)	4.83	5.34	5.51
Inferred Mass (kg)	33.6	8.4	61.3

To demonstrate the utility of combined observations for trajectory characterization, we also analyzed seismoacoustic observations. Clemente et al. (2025) found seismic signals that matched the length, frequency and waveform shape of a ballistic trajectory signal at 13:56:14z. Four seismic stations in Victoria (BRAT, GVL, GEXS and TOO) recorded a single signal (Fig. 10) during bright flight, while two stations in Tasmania recorded a double (CORO) and single (GLAD) signal during dark flight (Fig. 11). In contrast to ballistic shock-waves that propagate perpendicular to the trajectory, fragmentation or airburst shock-waves propagate quasi-spherically. No fragmentation or airburst shock-waves were detected (Clemente et al., 2025). The implications of these results for fragmentation and re-entry characterization are discussed in Section 5.3.

In addition to seismoacoustic observations, we received three ballistic trajectory signals from the I05AU infrasound array in Tasmania. We assume that these signals were caused by multiple objects each generating their own shock-wave as it is highly likely that the object fragmented over the Bass Strait (outside the sensing range of the ANSN). We estimated source origins and inferred masses through array processing which is shown in Table 5. Signal 1 was the strongest and indicated an inferred mass of 33.6 kg traveling at 4.8 km/s. We treated m_{inf} as a lower bound for m, approximating $m_{inf} \approx m$ and used this endpoint to initialize a second dark flight trajectory. The column “Infrasound” in Table 6 captures the endpoint parameters to predict pure dark flight, i.e., excluding the extended portion of bright flight over the Bass Strait as in the case of our main trajectory solution. We ran one thousand Monte Carlo simulations, varying the starting mass, density and shape factor by 25 kg, 500 kg/m^3 and 1 ± 0.15 to reflect the assumption that the object fragmented and now has a flat plate shape factor. The average surviving mass was 46 kg and our lower and upper estimates were 28.59 kg and 95.56 kg. All simulations splashed down within the designated NOTAM danger area around 14:01:28z, shown in Fig. 12.

Finally, we used the endpoint of our segment 2 (middle) bright flight trajectory to initialize a third dark flight trajectory. The column “Segment 2” in Table 6 captures the endpoint parameters to initialize dark flight with an extended portion of bright flight, i.e., including the whole of segment 3. We calculated a realistic initial mass, ran Monte Carlo simulations similarly to our main solution and received a similar average surviving mass (Table 6), but a fall zone that extended a further 1380 km south-east from our main solution, as shown in Fig. 13. Most simulations splashed down within the designated NOTAM danger area around 14:04:00z, as shown in Fig. 13.

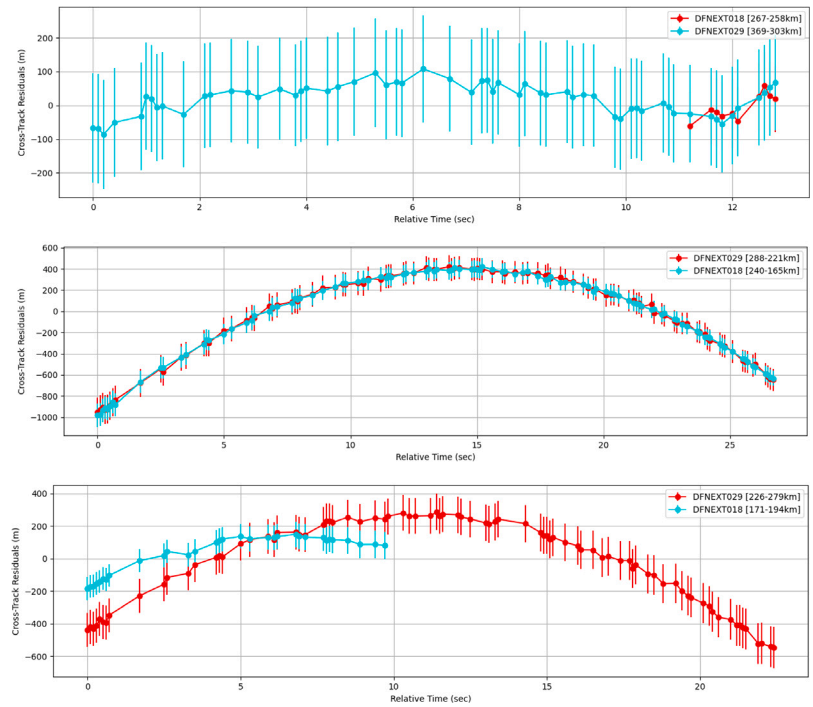

Fig. 8. Reduced cross-track residuals for our main trajectory solution across segments 1 (top), 2 (middle) and 3 (bottom). The label includes observing camera name and distance range to the fireball.

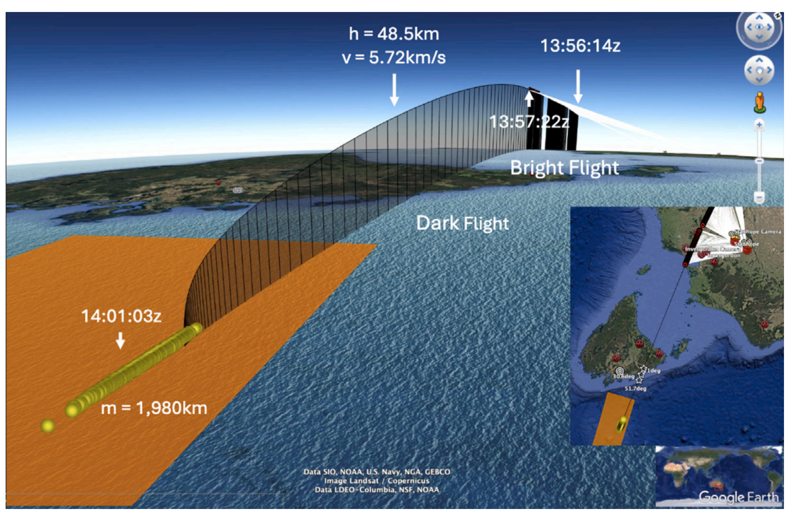

Fig. 9. End-to-end trajectory solution, including bright and dark flight between 13:57:22z–14:01:03z. All surviving mass simulations (yellow points) splashed down within the designated NOTAM danger area (orange polygon). (For interpretation of the references to color, the reader is referred to the web version of this article.)

Table 6
Endpoint parameters used to predict our main, pure dark flight (Infrasound) and extended bright (Segment 2) trajectory paths, as well as average surviving masses and impact areas.

Parameter	Main	Infrasound	Segment 2
Initial Mass (kg)	2,041 ± 500	33.6 ± 25	2,784.36 ± 500
Density (kg/m^3)	2,813 ± 500	2,813 ± 500	2,813 ± 500
Shape Factor	0.6–1.6	1 ± 0.15	0.6–1.6
Height (km)	64.13	37.3	69.82
Velocity (km/s)	6.29	4.83	7.38
Zenith Distance (°)	88.57	85.45	90.1
Flight Path Angle (°)	−1.43	−4.55	0.1
Azimuth (°)	142.65	140.37	146.93
Average Surviving Mass (kg)	1,980	46	2,134
Average Latitude/longitude	−43.24,149.93	−43.29, 149.96	−52.23,161.34

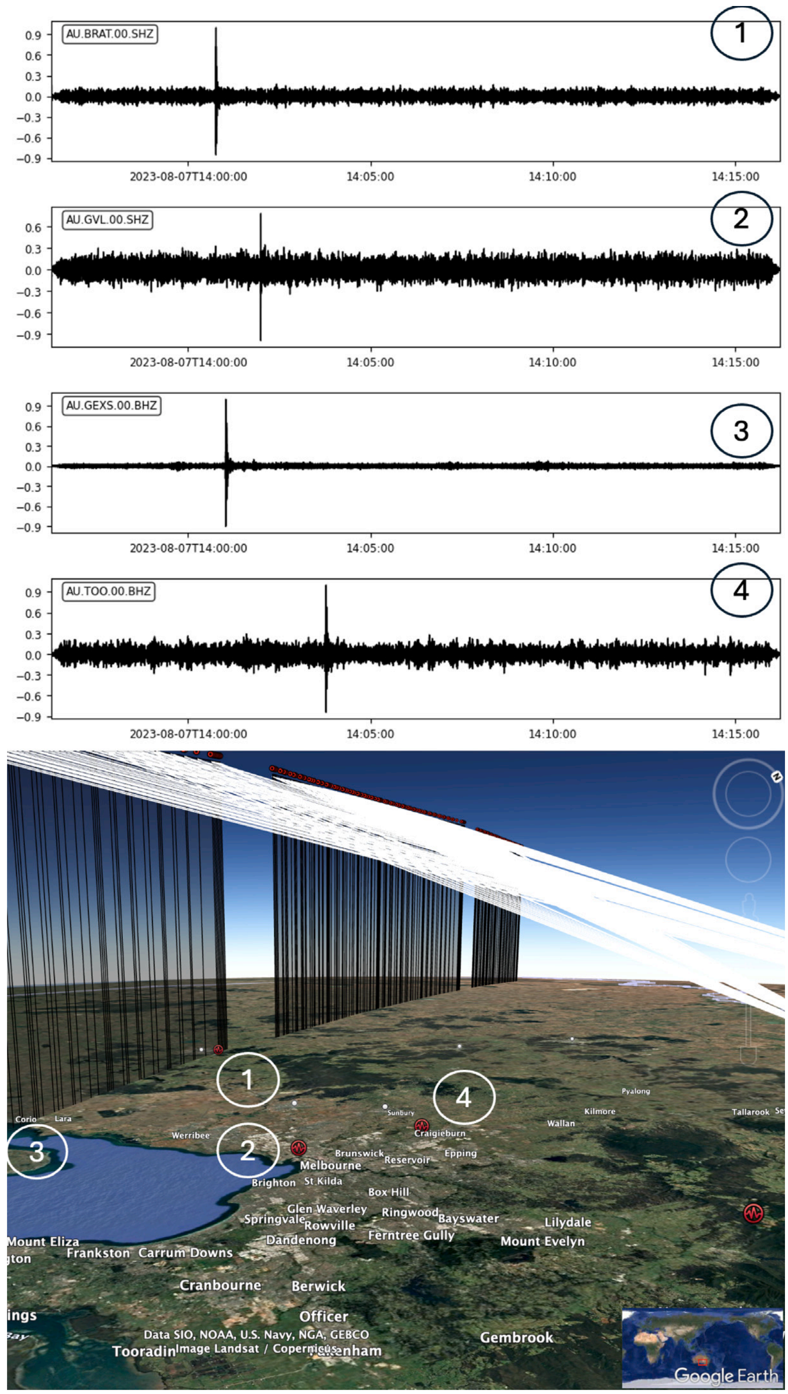

Fig. 10. Seismic timeseries data from BRAT (1), GVL (2), GEXS (3) and TOO (4) seismic stations around Victoria, showing distinctive signals that are consistent with a ballistic trajectory during bright flight of the Soyuz-2.1b re-entry.

5.3. Discussion

The DTF method with minor modifications successfully reconstructed bright flight and initialized dark flight to verify splashdown of a Soyuz-2.1b second stage within the designated NOTAM danger area. Here we discuss key trends in our results, namely cross-track deflection, suspected fragmentation and survivability for further characterization.

5.3.1. Cross-track deflection

Cross-track residuals are defined as the angular difference between the predicted and observed lines of sight, measured perpendicular to the apparent velocity vector from the sensor's perspective. The severe cross-track deflection that we see in our global trajectory solution indicates the presence of one or more unmodeled forces acting on the object. Segmenting the trajectory substantially improved velocity estimates and reduced cross-track residuals to less than 1 km, enabling dark flight initialization. We acknowledge that a segmented trajectory solution does not fully capture the true trajectory uncertainty, and that alternative trajectory reconstruction methods—such as Unscented Kalman Filters (Sansom et al., 2015) or 3D particle filters (Sansom et al., 2018)—may be more suitable. The segmented trajectory solution's failure to capture the true trajectory is evident in the large cross-track residuals and position error of segment 2 (Fig. 8). These errors lead to a positive zenith distance of 90.1° at the final observation

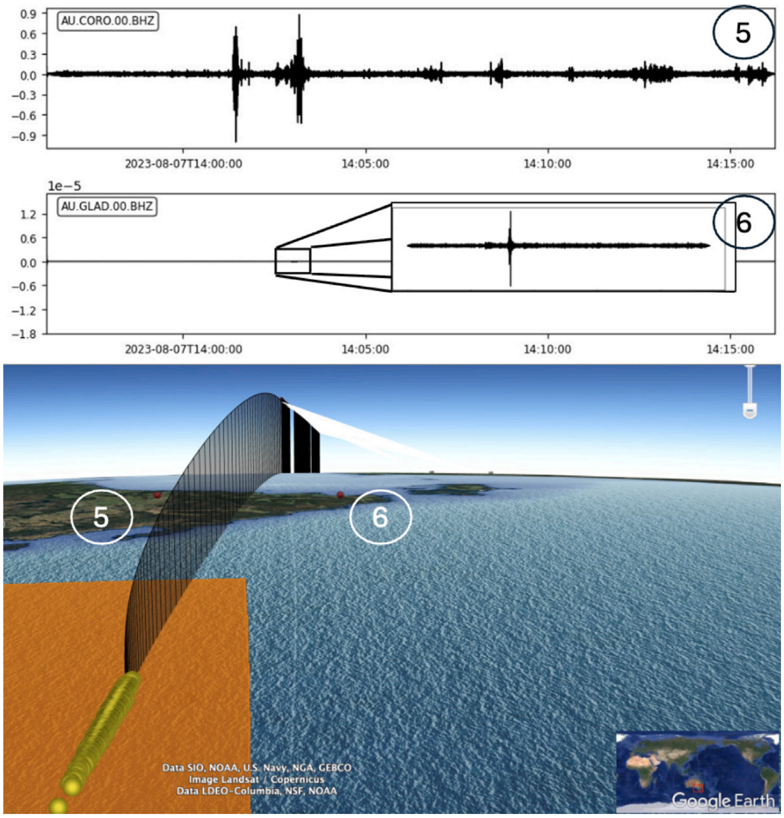

Fig. 11. Seismic timeseries data from stations in Tasmania: CORO (5) and GLAD (6). A double seismic signature can be seen in CORO, and a single in GLAD. Signals are consistent with ballistic trajectories during dark flight of the Soyuz-2.1b re-entry.

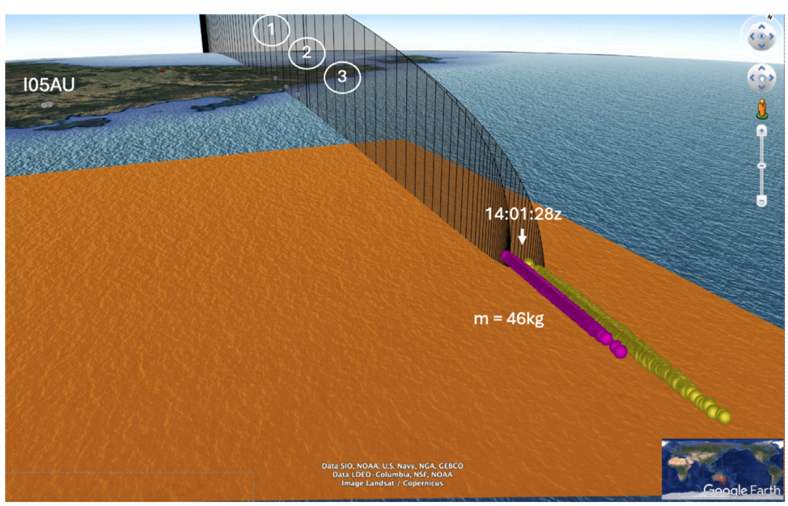

Fig. 12. Pure dark flight (Infrasound) trajectory path using an inferred mass of 33.6 kg. All surviving mass simulations (pink points) splashed down within the designated NOTAM danger area (orange polygon). (For interpretation of the references to color, the reader is referred to the web version of this article.)

point of segment 2, causing the fall zone to extend a further 1380 km south-east of our main solution. Although an alternative model may be more suitable, the DTF method is sufficient for verifying splash-down and exploring the sensitivity of physical parameters, provided observations extend towards the end of bright flight and can be further constrained using complementary, interdisciplinary observations.

Our trajectory solution using the minimum cross-sectional area, i.e., falling face-down, produced the smallest cross-track residuals, but resulted in a completely ablated object with a final mass of 0 kg over Victoria. The associated high deceleration is inconsistent with both observations and ballistic trajectory signals observed over Tasmania. In the absence a model capable of specifying different attitude modes, such as random tumbling, tumbling about a fixed axis, or stable attitude (Pontijas Fuentes et al., 2019), we adopt the maximum projected cross-sectional area as a conservative upper bound on aerodynamic drag for a tumbling object. Accordingly, our main solution assumes the

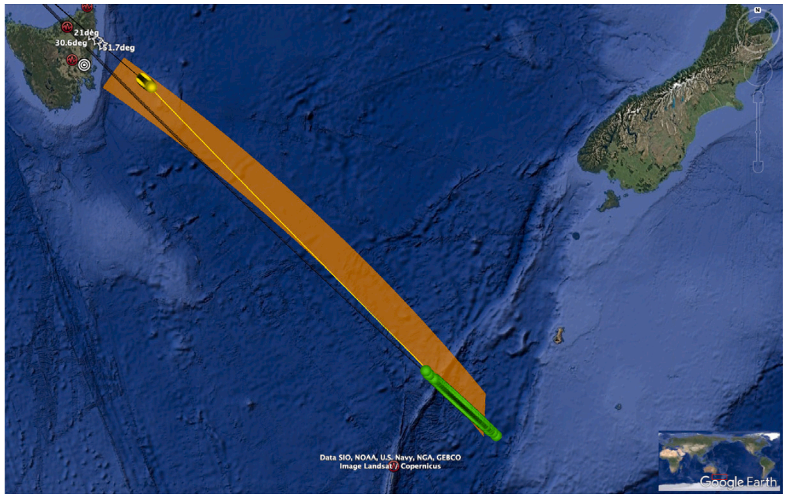

Fig. 13. Fall zone for the extended bright flight (Segment 2) trajectory path (green points), extended a further 1380 km south-east from our main solution (yellow points). Both solutions fall within the NOTAM danger area (orange polygon). (For interpretation of the references to color, the reader is referred to the web version of this article.)

maximum cross-sectional area, i.e., a cylinder falling side-down, as this configuration yields deceleration and mass estimates consistent with observations.

A cylinder falling side-down or horizontally could also experience the Magnus effect, curving its trajectory due to its spin. This force would be more prominent for longer duration segments as seen in Table 3. An order-of-magnitude estimate shows that Magnus-induced lift arising from realistic spin rates produces accelerations on the order of ∼0.051 m/s^2 during segment 3. Although this is significantly smaller than atmospheric drag at that altitude (∼21.7 m/s^2), such forces are nonetheless sufficient to generate kilometer-scale cross-track deflections over the observed bright flight duration. The velocity was also increasing for the duration of segment 1 and decreasing for segments 2 and 3. Deceleration is expected when atmospheric drag overcomes acceleration due to gravity at lower altitudes. Given that atmospheric drag was larger than the acceleration due to gravity during segment 1, the increasing velocity suggests that lift may be the cause of momentary acceleration. However, we must note that only one camera was observing at the beginning and end of the DFN's observation window with unideal convergence angles (8°), introducing uncertainty to these results. Future work will focus on determining which method best fits the line-of-sight observations, while also incorporating lift effects to improve the overall fidelity of results.

5.3.2. Suspected fragmentation

Data captured by the DFN over Victoria shows no sharp changes in deceleration that would indicate fragmentation points. Single signals consistent with a ballistic trajectory from four seismic stations over Victoria also suggest that fragmentation during the DFN observation window was unlikely (Clemente et al., 2025). We therefore did not model fragmentation using the DTF method. However, video camera footage captured by eyewitnesses in the outer suburbs of Melbourne clearly shows several fragments around the main fireball (Fig. 14). This footage was captured towards the end of the DFN's observation window, as the fireball was heading over the Bass Strait. Our final exposure image from Invergordon showed brightness flares consistent with fragmentation at the very end of the DFN's observation window (Fig. 3). Our deceleration curve may not have shown signs of fragmentation due to the uncertainty introduced by only one observing camera.

Space debris re-entry modeling tools, such as the European Space Agency's Debris Risk Assessment and Mitigation Analysis (DRAMA) software suite, commonly assume a fixed breakup altitude of 78 km (Pontijas Fuentes et al., 2019). However, our observations indicate suspected fragmentation at an altitude of 64 km. The thermal criterion, which triggers fragmentation when the surface temperature reaches a specified threshold, e.g., melting temperature, is generally considered more accurate than a fixed-altitude assumption (Wu et al., 2011; Parigini et al., 2017). More bespoke models also consider the balance between incoming aero-thermal heating and radiative heat loss to estimate breakup, allowing for a more realistic representation of the evolving mass, cross-sectional area, and temperature during re-entry (Pontijas Fuentes et al., 2019). Although our observations at the very end of the DFN's observation window are limited and do not allow us to model fragmentation using the DTF method, we aim to incorporate the thermal criterion into our ablation modeling, following the approach of Bartková et al. (2024) and Zigo et al. (2025). This is expected to further improve the representation of lift effects and accuracy of true mass estimates of fragments for comparison with inferred masses.

The two signals observed by the CORO seismic station (Fig. 11) and three signals by the I05AU infrasound array (Table 5) may suggest the presence of up to three ballistic fragments over Tasmania. The leading fragment with an inferred mass of 33.6 kg produced the strongest signal, indicating early separation of a compact and stable fragment, such as an avionics or instrumentation unit. The following fragment with an inferred mass of 8.4 kg produced a weak signal, indicating an unstable fragment with a large cross-sectional area-to-mass ratio, such as a thin aluminum panel or tank shell fragment. Finally, the trailing fragment with an inferred mass of 61.3 kg indicates late separation and sharp deceleration or reorientation that increased acoustic energy relative to its size, consistent with a dense engine-related component, such as a turbo-pump or thrust-frame hardware. Fragment ordering is consistent with gradual fragmentation and reflects both separation timing and ballistic coefficient.

5.3.3. Survivability

Our main trajectory solution assumes that the Soyuz-2.1b can be represented as an aluminum alloy cylinder falling side-down in a continuum flow. Cross-sectional area was found to be the most sensitive physical parameter for survivability estimates. The DTF method assumes a constant shape factor which is valid for a circular cylinder with a cross-sectional diameter to length ratio of 1:1, but it is not valid in this case due to a ratio of 1:9 (Sansom et al., 2015). However, our reasonable true mass estimates suggest that the orientation remained largely constant throughout bright flight in this case. As discussed in Sections 5.3.1 and 5.3.2, incorporating the thermal criterion into our

Fig. 14. Image of the Soyuz-2.1b re-entry captured by an eyewitness in the outer suburbs of Melbourne (ABC News, 2023).

ablation modeling is expected to improve the accuracy of true mass estimates of fragments for comparison with inferred masses.

Although true mass estimates of fragments are unknown, avionics or instrumentation units, turbo-pumps and thrust frames can range between 200–1500 kg. This is consistent with an overall average surviving true mass estimate of 1980 kg and gradual fragmentation over the Bass Strait that separated the object into at least three main fragments. There was negligible risk to people and property due to the height and velocity of the objects over Victoria (65 km and 6.77 km/s) and Tasmania (48.5 km and 5.72 km/s). All objects splashed down within the designated NOTAM danger area around 14:01:03z.

6. Conclusion

With tens of thousands of satellites expected to be launched by 2050, the risk of falling space debris to people and property is growing. Scheduled re-entries rely on NOTAMs for risk assessment, but with no global standard for NOTAM generation, they often go unverified due to a global lack of observational coverage below 200 km. The DFN, coupled with the ANSN and the Australian infrasound network, have the only accurate record of a scheduled Soyuz-2.1b second stage re-entry over Australia, providing multiple source verification and rare suborbital truth data for NOTAM verification. We estimated an overall average surviving mass of 1980 kg with gradual fragmentation over the Bass Strait that separated the object into at least three main fragments. There was negligible risk to people and property due to the height and velocity of objects over Victoria (65 km and 6.77 km/s) and Tasmania (48.5 km and 5.72 km/s). All objects splashed down within the designated NOTAM danger area around 14:01:03z on 7 August 2023, 4 min and 48.5 s after our first observation. Future work will focus on determining which method best fits line-of-sight observations across multiple case studies, while incorporating lift effects to improve overall fidelity. We also plan to incorporate the thermal criterion into our ablation modeling, which is expected to further improve the representation of lift effects and accuracy of true mass estimates of fragments for comparison with inferred masses. As more and more satellites are launched into orbit, there is an increasing need for monitoring, highlighting the value of high accuracy risk assessments using inter-disciplinary observations for re-entry verification.

CRediT authorship contribution statement

Isabella R. Hatty: Writing – review & editing, Writing – original draft, Visualization, Software, Methodology, Investigation, Formal analysis, Conceptualization. **Eleanor K. Sansom:** Writing – review & editing, Writing – original draft, Supervision, Software, Methodology, Investigation, Formal analysis, Conceptualization. **Hadrien A.R. Devillepoix:** Writing – review & editing, Supervision, Software, Methodology, Investigation, Formal analysis, Data curation, Conceptualization. **Trent Jansen-Sturgeon:** Writing – review & editing, Supervision, Software, Methodology, Formal analysis. **Martin C. Towner:** Writing – review & editing, Software, Methodology, Formal analysis, Data curation. **Iona Clemente:** Writing – review & editing, Methodology, Investigation, Formal analysis, Data curation.

Declaration of competing interest

The authors declare that they have no known competing financial interests or personal relationships that could have appeared to influence the work reported in this paper.

Acknowledgments

The authors acknowledge the use of data from the Desert Fireball Network (DFN), which is funded by the Australian Research Council as part of the Australian Discovery Project scheme (DP170102529, DP200102073, DP230100301), the Linkage Infrastructure, Equipment and Facilities scheme (LE170100106), and receives institutional support from Curtin University.

The authors acknowledge Thomas W. C. Stevenson for useful discussions and input during the development of this work.The authors also thank the volunteer onsite operators at Invergordon and Stanhope for the operation and maintenance of the Victorian camera systems.

The authors futher acknowledge the use of data from the International Monitoring System (IMS) operated by the Comprehensive Nuclear-Test-Ban Treaty Organization (CTBTO). The data used in this study are available directly from CTBTO virtual Data Exploitation Center (vDEC). Data access can be granted upon request, following signature of a contract after necessary approvals have been secured. The views expressed in this paper are those of the authors and do not necessarily reflect the views of the CTBTO Preparatory Commission.

References

ABC News, 2023. Russian rocket parts likely cause of dazzling display over Australia's night sky, authorities say. https://www.abc.net.au/news/2023-08-08/space-junk-leaves-trail-across-melbourne-sky/102700674. (Accessed: 06 January 2025).

Bartková, D., Šilha, J., Tóth, J., Paprskárová, M., Matlovič, P., Zigo, M., Hrobár, T., Lemmens, S., Jilete, B., 2024. Event reconstruction of long march 3B rocket stage re-entry observed by all-sky meteor orbit system. In: Proceedings of the International Astronautical Congress. pp. 1131–1143, Interactive Presentation IP.11. URL https://iafastro.directory/iac/archive/browse/IAC-24/A6/IP/. (Accessed: 06 January 2025).

Borovička, J., 1990. The comparison of two methods of determining meteor trajectories from photographs. Bull. Astron. Inst. Czech. 41, 391–396.

Bronshten, V.A., 1964. Problems of the Movement of Large Meteoric Bodies in the Atmosphere. National Aeronautics and Space Administration, Washington, DC.

Ceplecha, Z., 1987. Geometric, dynamic, orbital and photometric data on meteoroids from photographic fireball networks. Bull. Astron. Inst. Czech. 38, 222–234.

Clemente, I., Sansom, E.K., Devillepoix, H.A.R., Kawamura, T., Fernando, B.A., Garcia, R.F., Collet, O., 2025. Exploring seismic signal detection and source identification of atmospheric entries: The Hayabusa2 sample return capsule as a benchmark. Seismol. Res. Lett. 96, 2780–2795. http://dx.doi.org/10.1785/0220250032.

Devillepoix, H.A.R., Sansom, E.K., Bland, P.A., Towner, M.C., Cupák, M., Howie, R.M., Jansen-Sturgeon, T., Cox, M.A., Hartig, B.A.D., Benedix, G.K., Paxman, J.P., 2018. The dingle dell meteorite: A halloween treat from the main belt. Meteorit. Planet. Sci. 53, 2212–2227. http://dx.doi.org/10.1111/maps.13142.

Devillepoix, H.A.R., Sansom, E.K., Shober, P., Anderson, S.L., Towner, M.C., Lagain, A., Cupák, M., Bland, P.A., Howie, R.M., Hartig, B.A.D., Sokolowski, M., Benedix, G., Forman, L., 2022. Trajectory, recovery, and orbital history of the madura cave meteorite. Meteorit. Planet. Sci. 57 (7), 1328–1338.

Fernando, B.A., Mialle, P., Ekström, G., Charalambous, C., Desch, S., Jackson, A., Sansom, E.K., 2024. Seismic and acoustic signals from the 2014 interstellar meteor. Geophys. J. Int. 238, 1027–1039. http://dx.doi.org/10.1093/gji/ggae202.

Gan, N., Xiong, Y., Yee, I., 2024. Suspected Chinese rocket debris seen falling over village after launch, video shows. https://edition.cnn.com/2024/06/24/china/china-rocket-debris-falls-over-village-intl-hnk. (Accessed: 06 January 2026).

Howie, R.M., Paxman, J.P., Bland, P.A., Towner, M.C., Sansom, E.K., Devillepoix, H.A.R., 2017. Submillisecond fireball timing using de bruijn timecodes. Meteorit. Planet. Sci. 52, 1669–1682. http://dx.doi.org/10.1111/maps.12878.

Jansen-Sturgeon, T., Sansom, E.K., Devillepoix, H.A.R., Bland, P.A., Towner, M.C., Howie, R.M., Hartig, B.A.D., 2020. A dynamic trajectory fit to multisensor fireball observations. Astron. J. 160, 190. http://dx.doi.org/10.3847/1538-3881/abb090.

Kanzler, R., Lips, T., Fritsche, B., Bonetti, D., Pontijas Fuentes, I., Letterio, F., Vicario de Miguel, G., Blanco Arnao, G., Palomo, P., Parigini, C., Bunte, K.-D., Miller, A., Garms, C., Kebschull, C., Lemmens, S., 2019. Upgrade of DRAMA's Spacecraft Entry Survival Analysis Codes. Technical Report DUP-FR, ESA Contract No. 4000115057/15/D/SR, European Space Agency (ESA).

Kiseleva, M., 2022. Lotos-S1 #6 | soyuz 2.1b. https://everydayastronaut.com/lotos-s1-6-soyuz-2-1b-2/. (Accessed: 24 March 2026).

Lee, S.-E., Byun, Y.-I., Kim, D., Hwang, H., 2025. LEO space situational awareness optimization with multiple sensor systems. J. Space Secur. 2, 65–75. http://dx.doi.org/10.23386/joss.2025.2.1.006.

Neidhart, T., Miljković, K., Sansom, E.K., Devillepoix, H.A.R., Kawamura, T., Dimech, J.-L., Wieczorek, M.A., Bland, P.A., 2021. Statistical analysis of fireballs: Seismic signature survey. Publ. Astron. Soc. Aust. 38, e016. http://dx.doi.org/10.1017/pasa.2021.11.

Parigini, C., Cano, J.L., Haya-Ramos, R., 2013. Preliminary estimation of the footprint and survivability of the chelyabinsk meteor fragments. arXiv Preprint URL https://arxiv.org/abs/1304.2410 arXiv:arXiv:1304.2410.

Parigini, C., Pontijas Fuentes, I., Bonetti, D., Blanco Arnao, G., Riley, D., 2017. DEBRIS: an object-oriented code for footprint, survivability and risk assessment. In: Proceedings of the European Conference on Space Debris. URL https://conference.sdo.esoc.esa.int/proceedings/sdc7/paper/510.

Picone, J.M., Hedin, A.E., Drob, D.P., Aikin, A.C., 2002. NRLMSISE-00 empirical model of the atmosphere: Statistical comparisons and scientific issues. J. Geophys. Res.: Space Phys. 107, SIA 15–1–SIA 15–16. http://dx.doi.org/10.1029/2002JA009430.

Pontijas Fuentes, I., Bonetti, D., Letterio, F., Vicario De Miguel, G., Blanco Arnao, G., Palomo Pérez, P., Parigini, C., Lemmens, S., Lips, T., Kanzler, R., 2019. Upgrade of esa's debris risk assessment and mitigation analysis (DRAMA) tool: Spacecraft entry survival analysis module. Acta Astronaut. 158, 148–160. http://dx.doi.org/10.1016/j.actaastro.2017.12.001.

ReVelle, D.O., 1976. On meteor-generated infrasound. J. Geophys. Res. 81, 1217–1230. http://dx.doi.org/10.1029/JA081i007p01217.

ReVelle, D.O., 2008. Acoustic-gravity waves from bolide sources. Earth Moon Planets 102, 345–356. http://dx.doi.org/10.1007/s11038-007-9181-3.

Sansom, E.K., Bland, P.A., Paxman, J.P., Towner, M.C., 2015. A novel approach to fireball modeling: The observable and the calculated. Meteorit. Planet. Sci. 50, 1423–1435. http://dx.doi.org/10.1111/maps.12478.

Sansom, E.K., Bland, P.A., Towner, M.C., Devillepoix, H.A.R., Cupák, M., Howie, R.M., Jansen-Sturgeon, T., Cox, M.A., Hartig, B.A.D., Paxman, J.P., Benedix, G.K., Forman, L., 2020. Murrili meteorite's fall and recovery from kati thanda. Meteorit. Planet. Sci. 55, 2157–2168. http://dx.doi.org/10.1111/maps.13566.

Sansom, E.K., Jansen-Sturgeon, T., Rutten, M.G., Bland, P.A., Devillepoix, H.A.R., Howie, R.M., Cox, M.A., Towner, M.C., Cupák, M., Hartig, B.A.D., 2018. 3D meteoroid trajectories. Icarus 321, 388–406. http://dx.doi.org/10.1016/j.icarus.2018.09.026.

Sansom, E.K., Rutten, M.G., Bland, P.A., 2017. Analyzing meteoroid flights using particle filters. Astron. J. 153, 87–96. http://dx.doi.org/10.3847/1538-3881/153/2/87.

Silber, E.A., Brown, P.G., 2019. Infrasound monitoring as a tool to characterize impacting near-earth objects (NEOs). In: Le Pichon, A., Blanc, E., Hauchecorne, A. (Eds.), Infrasound Monitoring for Atmospheric Studies. Springer International Publishing, pp. 939–986. http://dx.doi.org/10.1007/978-3-319-75140-5_31.

Silber, E.A., Trigo-Rodríguez, J.M., Oseghae, I., Peña-Asensio, E., Boslough, M., Whitaker, R., Pilger, C., Lubin, P., Sawal, V., Hetzer, C., Longenbaugh, R., Jenniskens, P., Bailey, B., Mas Sanz, E., Hupe, P., Cohen, A.N., Edwards, T.R., Egan, S., Silber, R.E., Czarnowski, S.C., Ronac-Giannone, M., 2025. Multi-parameter constraints on empirical infrasound period-yield relations for bolides and implications for planetary defense. Astron. J. 170, 38. http://dx.doi.org/10.3847/1538-3881/add47d.

Šilha, J., Bártková, D., Kyselica, D., Matlovič, P., Tóth, J., Ďurikovič, R., Jevčák, P., Poláček, P., Lemmens, S., Jilete, B., 2023. Analysis of re-entry event of CZ-3B r/b observed by all-sky meteor cameras AMOS. In: Proceedings of the NEO and Debris Detection Conference. URL https://conference.sdo.esoc.esa.int/proceedings/neosst2/paper/19.

Skamarock, W.C., Klemp, J.B., Dudhia, J., Gill, D.O., Barker, D.M., Duda, M.G., Huang, X.-Y., Wang, W., Powers, J.G., 2008. A Description of the Advanced Research WRF Version 3. Technical Report NCAR/TN-475+STR, National Center for Atmospheric Research, http://dx.doi.org/10.5065/D68S4MVH.

Space-Track.Org, 2026. Space-track.org. https://www.space-track.org/auth/login. (Accessed: 06 January 2026).

The Aerospace Corporation, 2026. Reentries. https://aerospace.org/reentries. (Accessed: 06 January 2026).

Towner, M.C., Sansom, E.K., Cupak, M., Devillepoix, H.A.R., Anderson, S., Shober, P., Howie, R.M., Hartig, B.A.D., Bland, P.A., 2021. The Australian desert fireball network: Overview and recent results. Eur. Sci. Congr. EPSC2021, EPSC2021–167. http://dx.doi.org/10.5194/epsc2021-167.

Vovk, M., Koschny, D., Frühauf, M., Gscheidle, C., Hugentobler, U., Heumann, V., Lips, T., Fritsche, B., Maigler, M., Pessina, V., Šilha, J., Tóth, J., Pazderová, V., Matlovič, P., 2023. Meteoroid ablation simulations with esa's SCARAB software. Planet. Space Sci. 238, 105785. http://dx.doi.org/10.1016/j.pss.2023.105785.

Wright, E., Boley, A., Byers, M., 2024. Improving casualty risk estimates for uncontrolled rocket body reentries. J. Space Saf. Eng. 11, 74–79. http://dx.doi.org/10.1016/j.jsse.2024.01.004.

Wu, Z., Hu, R., Qu, X., Wang, X., Wu, Z., 2011. Space debris reentry analysis methods and tools. Chin. J. Aeronaut. 24, 387–395. http://dx.doi.org/10.1016/S1000-9361(11)60046-0.

Zak, A., 2025. The soyuz-2 rocket series. https://www.russianspaceweb.com/soyuz2_lv.html. (Accessed: 06 January 2026).

Zigo, M., Bartková, D., Šilha, J., Tóth, J., Lemmens, S., Jillet, B., 2025. Validation of the ESA statistical re-entry modelling tool DRAMA on ground-based optical data. In: Proceedings of the European Conference on Space Debris. URL https://conference.sdo.esoc.esa.int/proceedings/sdc9/paper/135.